



Article

# Patterns of Influence of Parallel Rock Fractures on the Mechanical Properties of the Rock–Coal Combined Body

Yakang Li, Jiangwei Liu \* and Qian Yu

College of Energy and Mining Engineering, Shandong University of Science and Technology, Qianwanggang Road 579, Qingdao 266590, China

\* Correspondence: jiangweiliu@cumt.edu.cn; Tel.: +86-0532-86057948

**Abstract:** Hydraulic fracturing of a roof can attenuate the strong mineral pressure and stress transfer by creating a series of parallel artificial fractures in it, and different forms of hydraulic parallel fractures have different effects on the attenuation effect of the coal rock system. In this regard, this study investigated the influence law of different forms of parallel pre-cracks on the mechanical properties of a rock–coal combined body through PFC<sup>2D</sup> numerical simulation, and the following conclusions were obtained. Parallel pre-cracks significantly affected the mechanical properties of the rock–coal combined body. The stress–strain curve of the coal–rock assemblage containing Parallel pre-cracks changes significantly following reductions in peak strength, peak strain, elastic modulus, and crack initiation stress. The closer the angle  $\theta$  between the single set of parallel pre-cracks and the horizontal is to  $30^\circ$ , the longer the length, L, and the lower the peak strength of the specimen, the peak strain, the modulus of elasticity, and the crack initiation stress. Macroscopic damage patterns are given for a rock–coal combined body containing single sets of parallel pre-cracks of different parameters, with coal sample damage, coal–rock sample damage and rock sample damage; a rock–coal combined body containing parallel pre-cracks is divided into three modes of fracture initiation when pressurized. These are the cracking of the coal sample, the simultaneous cracking of the parallel pre-crack tips in coal and rock samples, and the cracking of the parallel pre-crack tips in rock samples.



Citation: Li, Y.; Liu, J.; Yu, Q.

Patterns of Influence of Parallel Rock Fractures on the Mechanical Properties of the Rock–Coal Combined Body.

*Sustainability* **2022**, *14*, 13555.

<https://doi.org/10.3390/su142013555>

Academic Editors: Xiangguo Kong,  
Dexing Li and Xiaoran Wang

Received: 9 September 2022

Accepted: 17 October 2022

Published: 20 October 2022

**Publisher's Note:** MDPI stays neutral with regard to jurisdictional claims in published maps and institutional affiliations.



**Copyright:** © 2022 by the authors. Licensee MDPI, Basel, Switzerland. This article is an open access article distributed under the terms and conditions of the Creative Commons Attribution (CC BY) license (<https://creativecommons.org/licenses/by/4.0/>).

**Keywords:** pre-cracks; rock–coal combined body; hydraulic fracturing; crack initiation

## 1. Introduction

The deformation, transport, and breakage patterns of the roof plate during the coal mining face retrieval process can result in a mineral pressure phenomena. When the top plate is harder, the fracture of the hard top plate can easily cause strong dynamic pressure to appear [1–5]. The application of the hydraulic fracturing method can create artificial cracks in the rock formation, attenuate the strength of the rock formation, reduce the degree of stress concentration, ease the mine pressure, and reduce the possibility of the sudden release of energy, which is of great significance for the management of strong dynamic pressure roadways and impact ground pressure control [6–9]. Studies have shown that the spatial morphology of hydraulic fractures, including their length, direction, and density, significantly influences the attenuation of roof rocks [10,11]. Conventional experiments with a single fracture mostly simulate hydraulic fractures or primary rock fractures. However, in engineering practice, most of the hydraulic fracturing boreholes are arranged parallel to each other in the direction of the roadway. Furthermore, the fracturing method mostly employs segmented retreating fracturing, which produces nearly parallel fractures in the same stress environment, generally resulting in one or some parallel fractures [12–14]. The study of the mechanical laws of roof pre-cracking on the coal–rock assemblage, seeking to reveal the mechanism of damage to the coal–rock body under load, is of great significance for the application of hydraulic fracturing technology in the pre-fracturing of coal–rock seams to increase the penetration, pressure relief from the roof, and the recovery of released

top coal. Therefore, there is an urgent need to carry out physical experimental studies of parallel fractures in the roof on a rock-coal combined body.

Local and international scholars have conducted extensive research on the strength and damage characteristics of “coal–rock” structures. There are currently two main approaches to the study of coal–rock structural bodies. The first is the collection and processing of coal and rock samples into standard coal–rock combination specimens for uniaxial or triaxial testing in the laboratory. The second entails borrowing numerical simulation tools [15]. Chen et al. [16] assessed the effect of rock-to-coal height ratio on the uniaxial compressive strength, macroscopic damage cracking stress, and elastic modulus of the “roof–column” structural body, and that of the loading rate on the uniaxial compression damage of the combined coal rock, by numerical simulation. Guo et al. [17] analyzed the effects of different inclination angles of a rock–coal combined body on its overall deformation and damage, obtained its strength and damage mechanisms under uniaxial and triaxial compression conditions, and analyzed the effects of intersection inclination angles on its overall deformation and damage. Zuo et al. [18] analyzed the differences in the mechanical properties and impact propensities of different coal–rock assemblages. Zhang et al. [19] investigated the influence of the combination method on the mechanical characteristics and damage mechanisms of a rock–coal combined body. Bai et al. [20] sought to investigate the progressive failure characteristics and mechanisms of different kinds of sandwiched coal–rock specimens. Zhao and Xia et al. [21–23] investigated the mechanical behavior and damage characteristics of 3D-printed irregular columnar jointed rock masses under uniaxial, biaxial, and true triaxial actions.

Reyes et al. [24] studied the damage of two cracked rock specimens under uniaxial compression conditions, and Zhang et al. [25] used two-dimensional discrete element software to simulate the crack expansion process in single- and double-fractured rock samples, considering the size of the specimens and influencing factors such as the loading rate. Qian and Li [26] simulated the crack extension process and characteristics of single fractured rocks under bidirectional compression, and analyzed the influence of the surrounding pressure on the crack extension of the rocks. Yin et al. [27] used PFC fine-scale granular flow software to simulate uniaxial compression tests on single-nodular granite with different nodal lengths and inclination angles, in order to investigate the characteristics of crack initiation stresses and damage stresses, and to analyze the effects of nodal length and inclination angle on crack initiation stresses and damage stresses. Liu et al. [12] analyzed the effect of a single fracture in the roof on the uniaxial compression mechanical properties and damage characteristics of combined coal–rocks. Zhang [28] analyzed the effect of parallel double-cracked disc specimens on the cleavage damage process. Yang et al. [29–32] analyzed the law of the influence of the dip angle of coplanar double fissures on the crack evolution process, and studied the deformation and strength characteristics of interrupted prefabricated fractured rocks in different surroundings.

Previous research has focused on the mechanical properties of intact combined coal bodies and on combined coal bodies with fractures in parts of the coal seam. Fewer studies have been conducted on combined coal–rock bodies with rock sections containing cracks. Based on this, this paper simulates the uniaxial compression test of a coal–rock assemblage with parallel cracks in the rock body through PFC<sup>2D</sup> software, and analyzes the influence law of the angles and lengths of artificial cracks on the mechanical properties of the assembled coal–rock.

## 2. Project Background

As shown in Figure 1, in engineering practice, most hydraulic fracturing boreholes are arranged parallel to each other in the direction of the roadway. The fracturing method mostly employs segmented retreating fracturing, which produces nearly parallel fractures in the same stress environment, generally resulting in multi-parallel fractures.

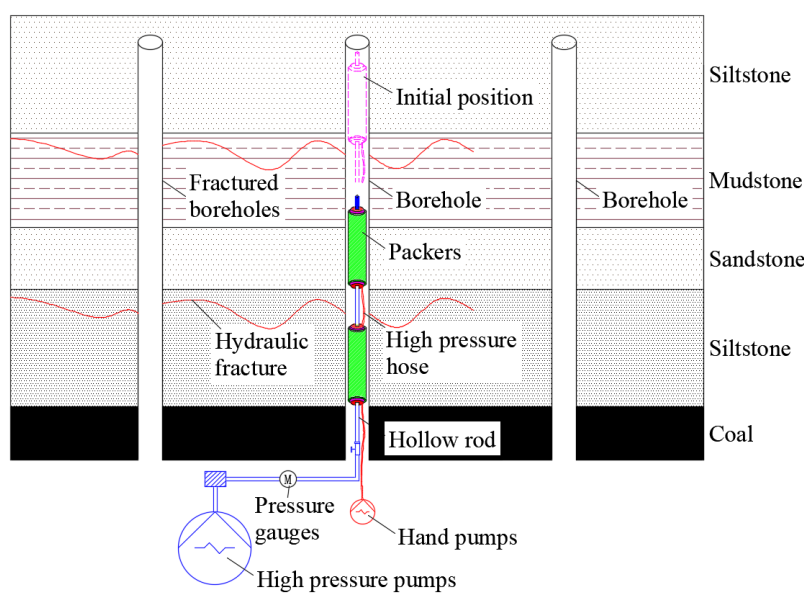


**Figure 1.** Schematic diagram of hydraulic fracturing in a coal mine.

As the roof of the working face is influenced by the weak coal seam underneath, the roof and coal seam should be considered jointly in the study of the damage evolution process of multi-parallel hydraulic fractures during loading, and the mechanical properties of the rock-coal combined body containing parallel hydraulic fractures, which can be used for the further analysis of the modification mechanism of the stress field.

### 3. Numerical Models

#### 3.1. Fine Mechanical Parameters of Coal and Rock

There are two main types of cohesive models in the PFC granular flow program: the parallel cohesive model can transfer forces and bending moments, and is therefore commonly used to simulate dense materials such as coal and rock [27,33–35].

Figure 2, and Tables 1 and 2, show that the results of the simulated specimens have small errors compared to those of the test specimens. Moreover, the final fine-scale parameters of the coal–rock can be used to study the effect of a single group of parallel pre-cracks on the mechanical properties of the combined coal rock.

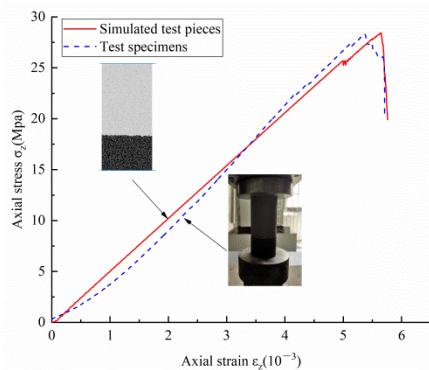


**Figure 2.** Comparison of stress–strain curves for simulated and test specimens.

**Table 1.** Comparison between results of simulated and test specimens.

	Peak Strength (MPa)	Peak Strain	Modulus of Elasticity
Simulated test pieces	28.438	0.00565	4.595
Test specimens	28.352	0.00537	4.666
Error	0.086	0.00028	-0.071

**Table 2.** Fine view parameters of coal and rock [33]. Note: Adapted from Liangfu Xie (2020).

Parameters	Rock	Coal	Parameters	Rock	Coal
Minimum particle size (mm)	0.2		Parallel bond elastic modulus (Gpa)	12	4
Particle size ratio	1.5		Parallel bond normal strength (Mpa)	45	15
Density ( $\text{kg}/\text{m}^3$ )	2533	1800	Parallel bond tangential strength (Mpa)	45	15
Contact modulus of the particle (Gpa)	12	4	Parallel bond normal stiffness/tangential stiffness	2.5	
Parallel bond radius multiplier		1	Normal stiffness/tangential stiffness	2.5	
Coefficient of friction			0.577		

Notably, the geometry of the prefabricated fractures simulated by the deleted particle approach depends on the microscopic material properties of the rock, and there is no need to recalibrate the microscopic parameters of the prefabricated fractures. Therefore, in this study, the results of physical experiments on the intact rock–coal combined body are used to determine microscopic parameters [36–39].

### 3.2. PFC<sup>2D</sup> Modeling

The model of the combined coal–rock is shown in Figure 3, with the rock in the upper part and the coal in the lower part. The specimen was 50 mm in diameter and 100 mm in height. According to the geological conditions of the Linhuan coal mine of Huabei Mining Company Limited, the thickness of the rock layer of the roof is 6.1 m and the thickness of the coal layer is 3.1 m. Therefore, the heights of the rock and coal parts of the specimen can be obtained according to an equiproportional calculation—the heights of the rock and coal were 67 mm and 33 mm, respectively. The model contained 15,129 rock particles and 7457 coal particles, all with particle radii ranging between 0.2 and 0.3 mm.

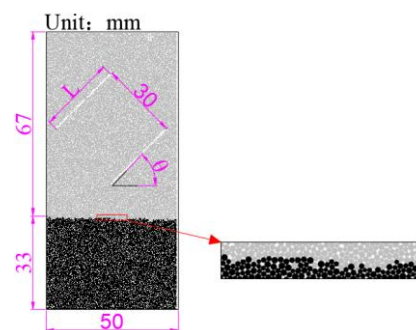


**Figure 3.** Numerical model of a coal–rock assemblage containing parallel pre-cracks.

Based on the available research results, the coal–rock interface was established, as shown in Figure 3. The friction factor at the coal–rock interface was taken as 0.1, the parallel bond normal and tangential stiffnesses were both 0, and the parallel bond normal and tangential strengths were both 0 [33,38].

### 3.3. Numerical Test Conditions

A parallel fracture was prefabricated in the rock sample of the rock–coal combined body. As shown in Figure 4, the widths of the hydraulic fractures in the field ranged from 0.1 to 1.5 mm; therefore, the width of this prefabricated fracture was determined to be 0.5 mm. Displacement loading was used, and the loading rate was set at 0.01 mm/s until the specimen broke. The specimen numbers and parameters were as follows:

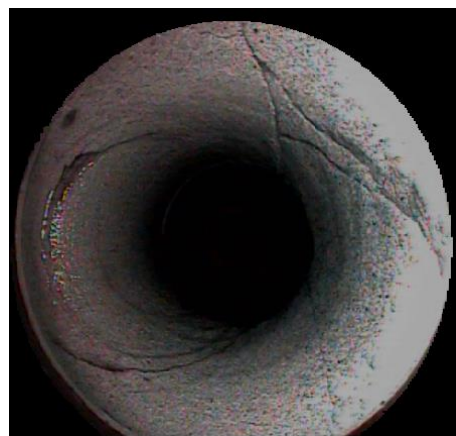


**Figure 4.** Hydraulic fracture patterns [40].

- (1) An intact coal–rock assemblage without parallel pre-cracks was set as the comparison specimen, as shown in Table 3 (1);
- (2) The length  $L$  was set as 30 mm and the crack spacing  $D$  as 30 mm, and a series of experiments with different crack angles  $\theta$  were conducted. The angles of  $\theta$  were  $0^\circ, 15^\circ, 30^\circ, 45^\circ, 60^\circ, 75^\circ$ , and  $90^\circ$ , as shown in Table 3 (2–8);
- (3) The crack angle  $\theta$  was set to  $45^\circ$  and the crack spacing  $D$  to 30 mm, and a series of experiments was carried out at different crack lengths  $L$ : 10, 15, 20, 25, 30, 35, and 40 mm, as shown in Table 3 (5, 9–14).

**Table 3.** Specimen parameters.

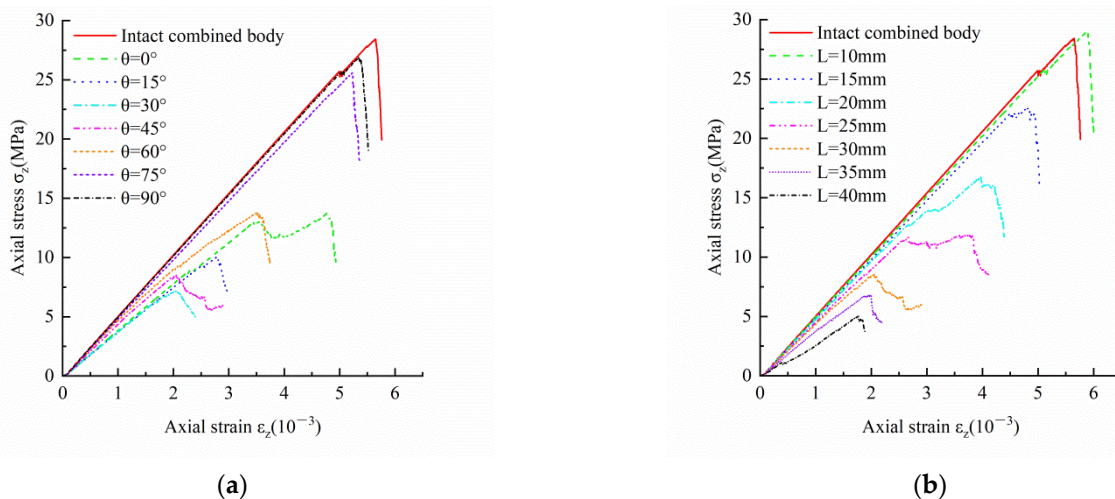
Specimen Number	Parallel Pre-Cracks Angle $\theta$ ( $^\circ$ )	Parallel Pre-Cracks Length $L$ (mm)
1	The intact rock–coal combined body	
2	0	30
3	15	30
4	30	30
5	45	30
6	60	30
7	75	30
8	90	30
9	45	10
10	45	15
11	45	20
12	45	25
13	45	35
14	45	40

#### 4. Patterns of Influence of Parallel Rock Fractures on the Mechanical Properties of the Rock–Coal Combined Body

##### 4.1. Effect of Parallel Pre-Cracks on the Stress–Strain Characteristics of the Rock–Coal Combined Body

As seen in Figure 5a, the slope of the stress–strain curve is the smallest for a parallel pre-crack angle  $\theta$  of  $30^\circ$ , and the peak strength and strain are significantly lower. Subsequently, the slope of the stress–strain curve, peak strength, and peak strain decreased for  $\theta = 15^\circ$  and  $45^\circ$ , respectively. For a  $\theta$  of  $90^\circ$  and  $75^\circ$ , the curves were similar to those of the intact specimens. The closer the angle of the parallel pre-cracks was to  $30^\circ$ , the lower the peak strength of the specimen, and the slower the slope of the stress–strain curve. From Figure 5a, it can be seen that the parallel pre-cracks with different angles had less influence on the line–elastic stage and compression–density stage of the specimen, and the stages with the most significant influence are the plastic stage and the damage stage, which is mainly

because, in the line-elastic stage and compression-density stage, we mainly focus on the elastic change of the specimen, which is related to the material properties of the specimen itself, and has little influence on the angle of the cracks. As the pre-crack is compressed to produce the crack, the expansion changes the plastic structure of the specimen before destruction, such that the specimen is influenced by the angle of the parallel pre-crack in the plastic stage and the destruction stage. From Figure 5b, the stress-strain curve slows down as the length  $L$  of the parallel pre-cracks increases. The stress-strain curve is slowest at an  $L$  of 40 mm, with the lowest peak strength and peak strain. The stress-strain curve at  $L = 10$  mm was close to that of the intact specimen, and the peak strength was higher than that of the intact specimen. As can be seen from Figure 5b, with a change in the length of the parallel pre-cracks, the stages with the most significant influence are mainly the line-elastic stage and the damage stage, which is mainly because the line-elastic stage and the pressure-density stage are mainly dominated by the elastic change of the specimen, which is related to the material properties of the specimen itself, and has little to do with the length of the cracks. As the pre-crack is compressed to produce a crack expansion that changes the plastic structure of the specimen before destruction, the specimen is affected by the lengths of the parallel pre-cracks in the plastic stage and the destruction stage.



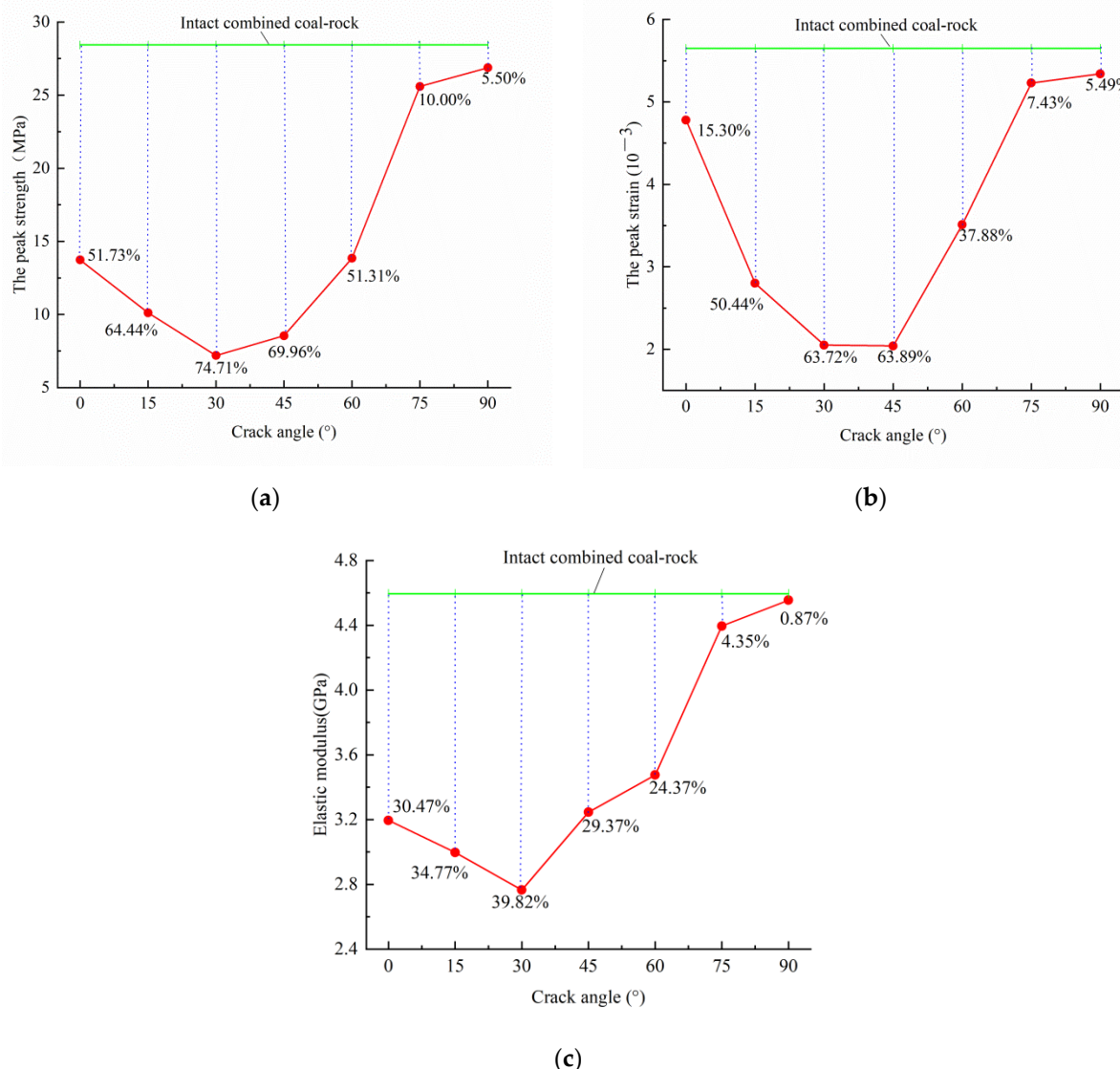
**Figure 5.** Stress–strain curves for the rock–coal combined body with parallel pre-cracks in different forms. (a) Stress–strain curves for different parallel pre-cracking angles. (b) Stress–strain curves for different parallel pre-crack lengths.

Figure 5 shows that the strain intervals corresponding to the compression–density and linear–elastic stages of the specimens with different parallel pre-crack parameters did not differ significantly, but the difference was greater after the elastic–plastic stage. The closer the parallel pre-crack angle  $\theta$  is to  $30^\circ$ , the greater the length  $L$  of the parallel pre-cracks, and the greater the change in the stress–strain curve relative to the intact specimen.

#### 4.2. Effect of Parallel Pre-Cracks on the Strength and Deformation Characteristics of the Rock–Coal Combined Body

As shown in Figure 6a, the peak strength decreased and then increased as the angle of the parallel pre-cracks increased. The peak strength of the rock–coal combined body is the smallest for a parallel pre-crack angle  $\theta$  of  $30^\circ$ , which is 74.71% lower than that of the intact specimen. This was followed by a reduction of 69.96% at a  $\theta$  of  $45^\circ$  compared to the intact specimen. As shown in Figure 6b, the peak strain first decreased and then increased as the angle of the parallel pre-cracks increased. At an angle  $\theta$  of  $45^\circ$ , the peak strain in the rock–coal combined body was the smallest, with a reduction of 63.89% compared to the intact specimen. This was followed by a reduction of 63.72% at a  $\theta$  of  $30^\circ$  compared to the intact specimen. As shown in Figure 6c, the modulus of elasticity first decreased and then increased as the angle of the parallel pre-cracks increased. The smallest modulus of

elasticity of the rock-coal combined body was seen at an angle  $\theta$  of  $30^\circ$ , with a decrease of 39.82% compared to the intact specimen. This was followed by a 34.77% drop at a  $\theta$  of  $15^\circ$  compared with the intact specimen. As shown in Figure 6, the peak strength, peak strain, and modulus of elasticity of the rock-coal combined body containing parallel pre-cracks at different angles were significantly reduced relative to the intact specimens. The closer the parallel pre-crack angle  $\theta$  is to  $30^\circ$ , the lower the peak strength, peak strain, and modulus of elasticity of the rock-coal combined body.



**Figure 6.** Effects of parallel pre-cracks at different angles on the strength of the rock-coal combined body. (a) Effect of parallel pre-cracks at different angles on axial stress. (b) Effect of parallel pre-cracks at different angles on axial strain. (c) Effect of parallel pre-cracks at different angles on elastic modulus.

As shown in Figure 7a, the peak strength decreased as the length  $L$  of the parallel pre-cracks increased. When the  $L$  was 40 mm, the peak strength decreased by 82.34% relative to that of the intact specimen. As shown in Figure 7b, the peak strain decreased as the length  $L$  of the parallel pre-cracks increased. When the  $L$  was 40 mm, the peak strain decreased by 68.67% relative to that of the intact specimen. As shown in Figure 7c, the modulus of elasticity decreased as the length  $L$  of the parallel pre-cracks increased. When the  $L$  was 40 mm, the peak strain decreased by 53.95% relative to that of the intact specimen. As shown in Figure 7, the peak strength, peak strain, and modulus of elasticity of the rock-coal combined body were significantly reduced by the different lengths of

parallel pre-cracks compared to the intact specimens. The peak strength, peak strain, and modulus of elasticity of the rock-coal combined body decreased as the length of the parallel pre-cracks continued to increase.

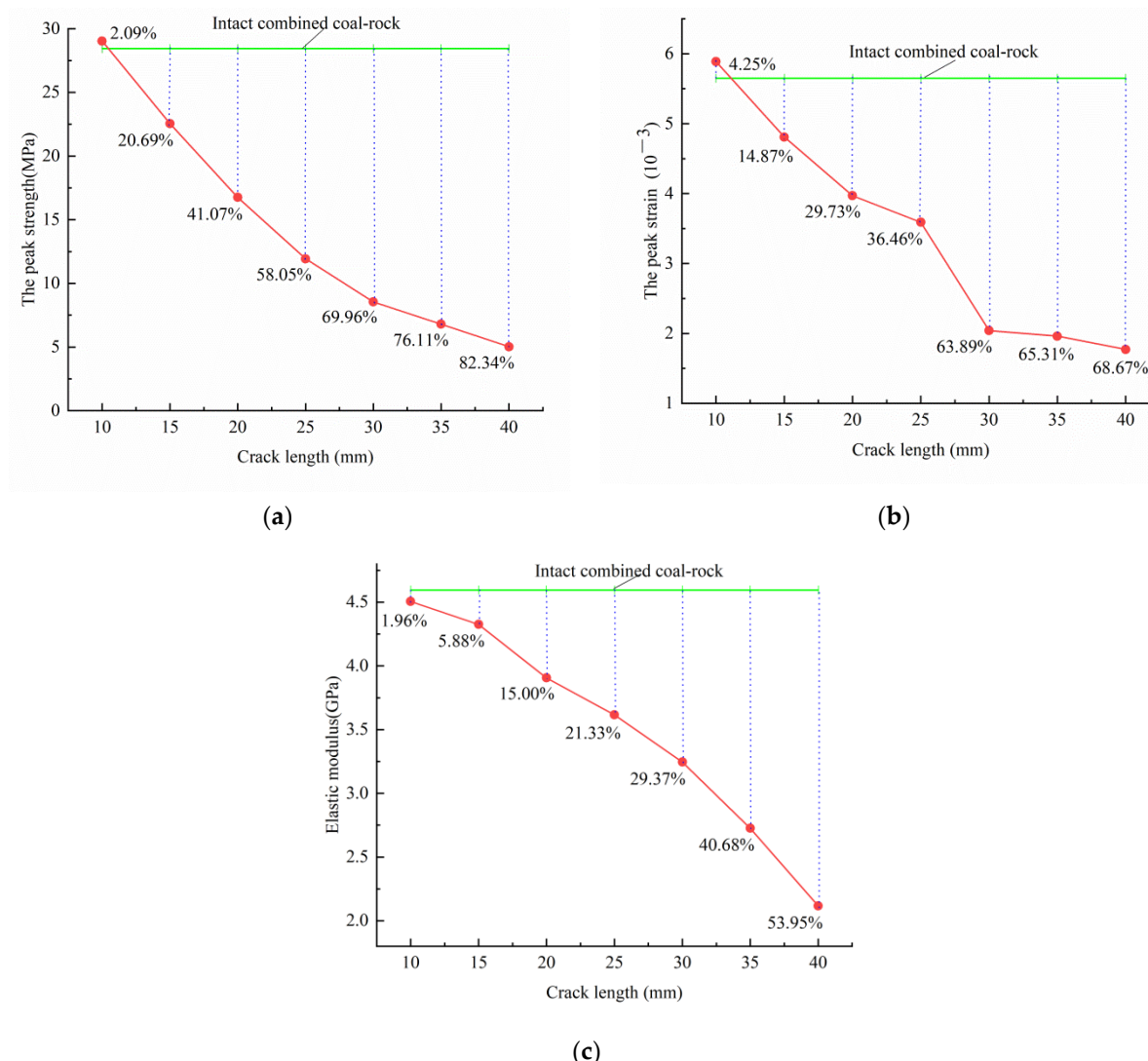


**Figure 7.** Effect of parallel pre-cracks of different lengths on the strength of the rock-coal combined body. **(a)** Effect of parallel pre-cracks of different lengths on the axial stress. **(b)** Effect of parallel pre-cracks of different lengths on axial strain. **(c)** Effect of parallel pre-cracks of different lengths on elastic modulus.

#### 4.3. Macroscopic Damage Characteristics of the Rock-Coal Combined Body by Parallel Pre-Cracks

In the following descriptions, the direction along the parallel pre-cracks is regarded as tangential, the direction perpendicular to the parallel pre-cracks as vertical, and the direction between the tangential and vertical as oblique. The final damage pattern of the rock-coal combined body with different parallel pre-cracks strains up to 0.01 is shown in Figures 8 and 9.

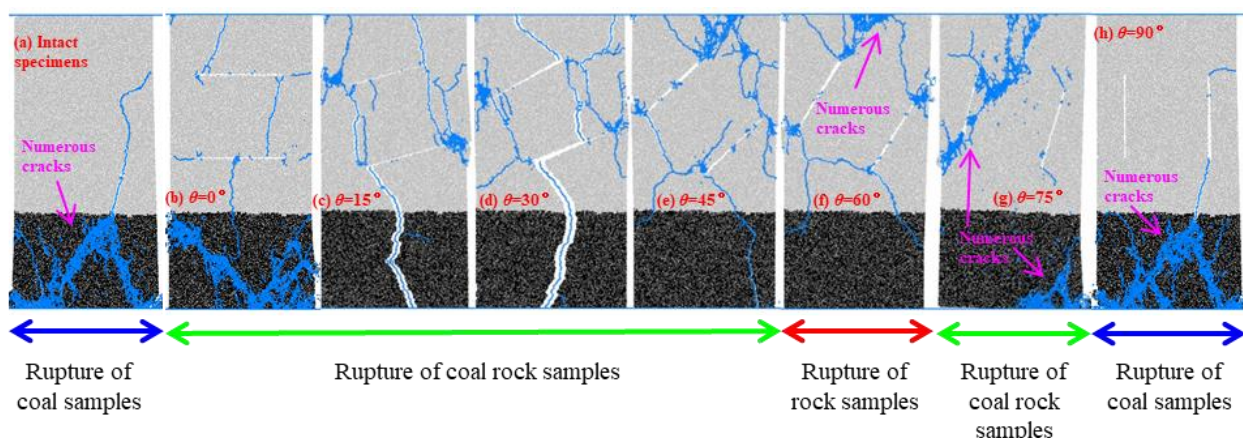


**Figure 8.** Macroscopic damage characteristics of parallel pre-cracks at different angles.

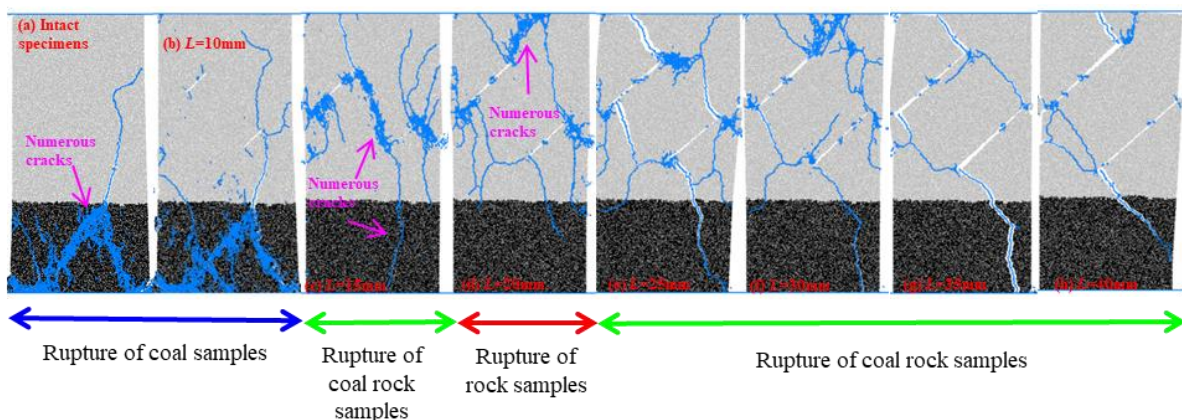


**Figure 9.** Macroscopic damage characteristics of parallel pre-cracks of different lengths.

Figure 8 shows that there are three macroscopic damage characteristics of the rock-coal combined body with different angles of parallel pre-cracks: coal rupture, rock and coal rupture, and rock rupture. As shown in Figure 8a,h, for intact specimens and  $\theta = 90^\circ$ , the coal samples in the rock-coal combined body exhibited more intensive cracking, the rock samples produced less cracking, and the damage occurred mainly in the coal samples. Figure 8b–e,g show that for  $\theta = 0^\circ$ ,  $\theta = 15^\circ$ ,  $\theta = 30^\circ$ ,  $\theta = 45^\circ$ , and  $\theta = 75^\circ$ , damage occurred in both the coal and rock samples, with more cracks around parallel pre-cracks and a reduced degree of damage in the coal samples relative to the intact specimens. At  $\theta = 15^\circ$ , the crack extended in the vertical direction, with the top end extending to the top of the specimen and the bottom end extending to the bottom of the specimen. At  $\theta = 30^\circ$ , parallel pre-cracks were observed along the vertical direction, and developed a major crack that destroyed the coal sample in the middle. It developed tangentially toward the boundary of the specimen and extended to the rock boundary, destroying the rock sample. At  $\theta = 45^\circ$ , parallel pre-cracks penetrated along the oblique direction, forming multiple oblique cracks that fractured the rock sample. Simultaneously, a number of seam networks were formed around the two parallel cracks, with certain cracks developing in the boundary to break the rock sample. At  $\theta = 75^\circ$ , an oblique crack extended along the direction of the parallel pre-cracks and produced a network of many seams. Destruction occurred at the bottom of the coal sample. As shown in Figure 8f, at  $\theta = 60^\circ$ , damage occurred mainly in the rock sample, with oblique damage to the rock and only a few small cracks in the coal body.

Therefore, the rock-coal combined body containing parallel pre-cracks at different angles exhibits three macroscopic damage patterns: coal sample rupture, coal-rock sample rupture, and rock sample rupture. As the parallel pre-crack angle  $\theta$  increases, the damage

pattern cycles from coal sample rupture to both coal and rock sample rupture, then to rock sample rupture, and back to coal sample rupture.

As shown in Figure 9, there are three macroscopic damage characteristics of the rock-coal combined body with different lengths of parallel pre-cracks: coal rupture, rock and coal rupture, and rock rupture. Figure 9a,b show that the form of damage of the rock-coal combined body for a parallel pre-crack length  $L$  of 10 mm is nearly identical to that of the intact specimen, occurring mainly in the coal sample, and a small amount of cracking occurred at the tip of the crack. As shown in Figure 9c, numerous seam networks were produced between the parallel pre-cracks and at the tips, and both the coal and rock samples ruptured, with the degree of rupture in the coal samples being significantly lower than that in the intact specimens. Figure 9d shows that the tips of the parallel pre-cracks penetrated each other, and the tips of the parallel pre-cracks produced a large network of seams, with damage occurring mainly in the rock samples. As shown in Figure 9e-h, the coal rock samples all fractured. Figure 9e,f show that the form of damage was essentially the same, except for the location whereat the seam network was created. Damage occurred preferentially in the rock samples and to a lesser extent in the coal samples. As shown in Figure 9g, a small seam network was produced, and the parallel pre-crack tips penetrated each other to form several main cracked damage specimens. As shown in Figure 9h, a small seam network was produced, and the tips under the parallel pre-cracks penetrated each other, preferentially breaking the rock sample in a tangential direction.

As shown in Figure 9, as the length  $L$  of the parallel pre-cracks increased, the rock-coal combined body, with different lengths of parallel pre-cracks, ruptured from only coal to both rock and coal, then to rock only, and finally cycled back to both coal and rock samples breaking.

#### 4.4. Effect of Parallel Pre-Cracks on the Fracture Initiation Pattern of the Rock-Coal Combined Body

As shown in Figure 10, the crack initiation stress of the rock-coal combined body containing parallel pre-cracks was reduced relative to that of the intact specimen. As the parallel crack angle  $\theta$  increased, the cracking stress in the rock-coal combined body with parallel pre-cracks decreased and then increased relative to the intact specimen. The greatest change in cracking stress was observed at a  $\theta$  of  $30^\circ$ , with a reduction of 72.15%. As shown in Figure 11, the parallel pre-cracks' initiation patterns at different angles can be divided into three types. The first type is shown in Figure 11a,h, with crack initiation in the coal sample. The second type is shown in Figure 11b,g, where the fracture started from both the tips of the parallel pre-cracks and the coal sample. The third type is shown in Figure 11c-f, with fracturing from the tip of the parallel pre-crack in the rock sample. As the angle  $\theta$  of the parallel pre-cracks increased, the rock-coal combined body cycled from coal to coal-rock simultaneously, then to rock-only initiation, and then to cracking from coal. When cracking from the tip of the parallel pre-crack, the direction of crack development gradually changed from vertical to tangential as the  $\theta$  increased.

As shown in Figure 12, the crack initiation pressure of the rock-coal combined body with parallel pre-cracks was reduced compared to that of the intact specimen. As the parallel pre-crack length  $L$  increased, the crack initiation stress decreased relative to the intact specimen. When the  $L$  was 40 mm, the crack initiation stress was minimized, with a reduction of 84.16% compared to the intact specimen. As shown in Figure 13, the crack initiation patterns of the specimens can be classified into three types. The first type is shown in Figure 13a, where the crack started from the lower end of the coal sample. The second type is shown in Figure 13b, where the crack started from both the tips of the parallel pre-cracks and the sample. The third type is shown in Figure 13c-h, where the crack started at the tips of the parallel pre-cracks.

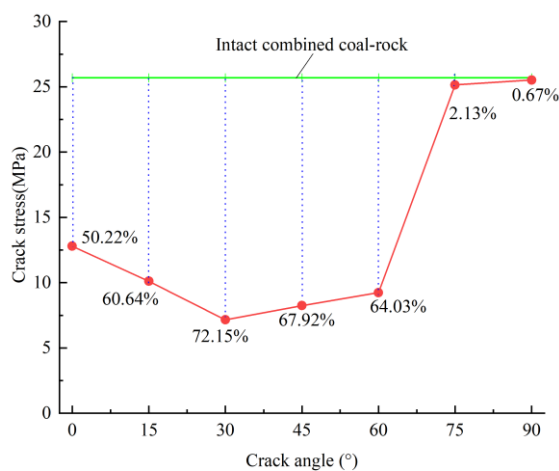


**Figure 10.** Crack stresses of parallel pre-cracks at different angles.

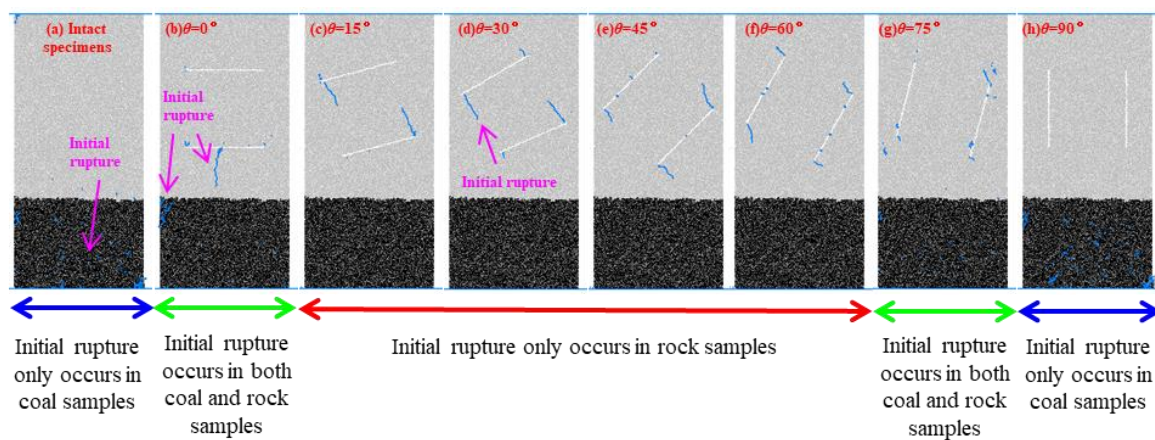


**Figure 11.** Rock–coal combined body initiation pattern with parallel pre-cracks at different angles.

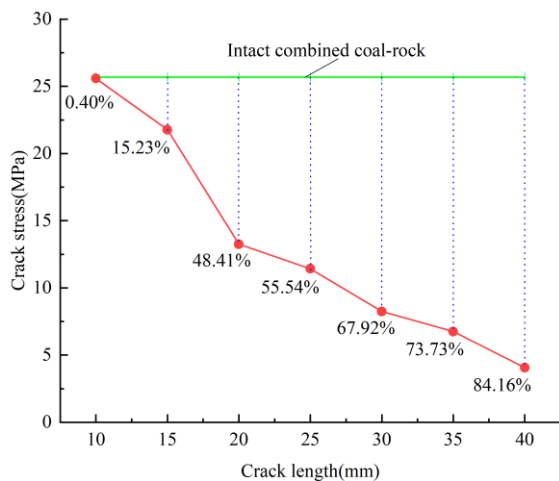


**Figure 12.** Crack stresses of parallel pre-cracks of different lengths.

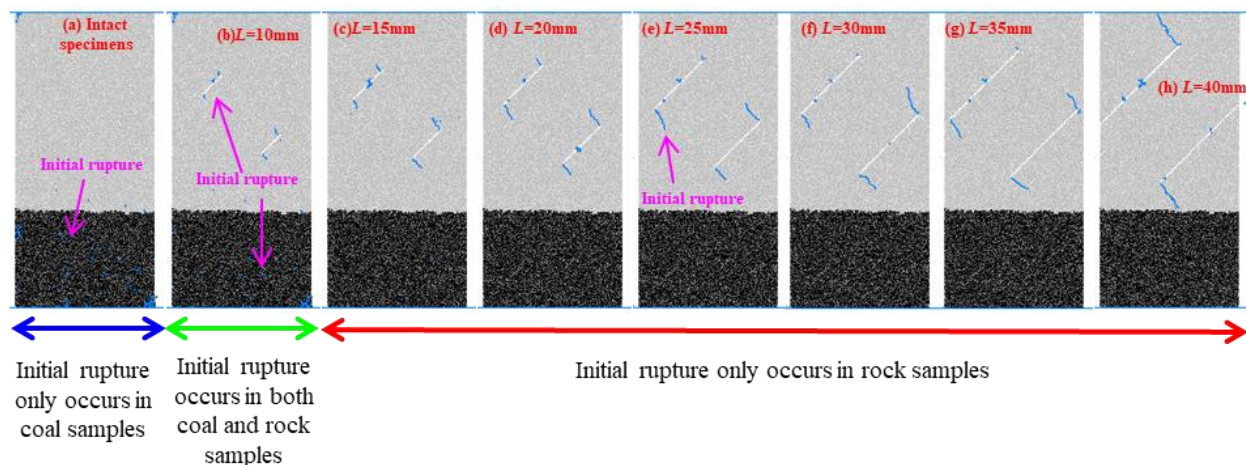


**Figure 13.** Rock–coal combined body initiation pattern with parallel pre-cracks at different lengths.

In summary, the rock–coal combined body with parallel pre-cracks exhibited three forms of crack initiation: crack initiation in the coal sample, simultaneous crack initiation at the tips of the parallel pre-cracks in the coal and rock samples, and crack initiation at the tips of the parallel pre-cracks in the rock sample. The highest crack initiation stress is required for the cracking of coal samples; the lowest crack initiation stress is required only for crack initiation at the tips of parallel pre-cracks in rock samples. The closer the angle of the parallel pre-cracks is to  $30^\circ$  and the longer the length, the lower the crack initiation stress. This study on the effects of parallel pre-cracks on fracture initiation pattern can be used to determine the parameters of hydraulic fractures in rock seams in practical engineering, to control the fracture initiation pattern and damage pattern of rock seams and lower coal seams, etc. For example, the effect on fracturing resulting from controlling the angle and length of the hydraulic fracture tip can make the rock seam rupture under pressure to absorb energy, so as to achieve the purpose of protecting the coal seam below.

#### 4.5. Effect of Parallel Pre-Cracks on Acoustic Emission Characteristics of the Rock–Coal Combined Body

From Figure 14, we see that the total number of acoustic emission events was highest at a parallel pre-crack angle of  $\theta = 90^\circ$  and lowest at  $\theta = 15^\circ$ . The overall change in the total number of acoustic emission events took the form of a gradual decrease and then a gradual increase as the angle  $\theta$  of the parallel pre-cracks changed. The rate of change of the acoustic emission phenomenon curve was the slowest at  $\theta$  of  $30^\circ$ , followed by  $15^\circ$ . This is because the acoustic emissions from intact specimens were mainly concentrated in the coal sample area, with the total number of acoustic emission events becoming smaller and then larger as the parallel pre-crack angle increased to  $45^\circ$ , before the acoustic emissions from the coal sample became progressively smaller and the acoustic emissions from the rock sample gradually increased. The number of acoustic emission events decreased in the rock samples and increased in the coal samples as the angle of parallel pre-cracks increased from  $45^\circ$  to  $90^\circ$ , with the total number of acoustic emission events first decreasing and then increasing. When  $\theta$  was  $90^\circ$ , the total number of acoustic emission events increased relative to that of the intact specimen. This is due to the fact that the coal specimens had almost identical fracture patterns, while the initiation of fracture tips in the rock samples increased the total number of acoustic emission specimens.

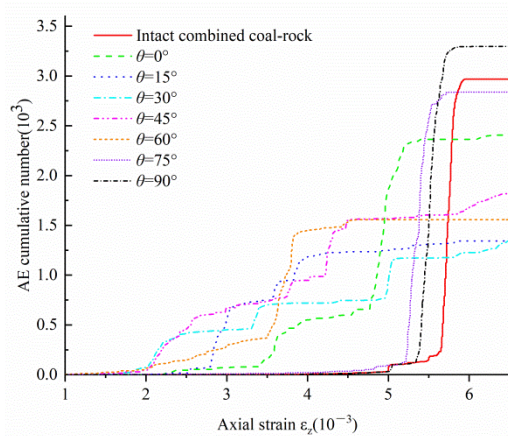


**Figure 14.** Effects of parallel pre-cracks at different angles on acoustic emission characteristics.

As shown in Figure 15, the total number of acoustic emission events was higher than that in the intact specimen when  $L$  was 10 mm, and both produced acoustic emissions at almost the same time. However, owing to the effects of parallel pre-cracks, the number of cracks produced in the rock sample was almost the same; however, owing to the effects of parallel pre-cracks, the number of cracks produced in the rock sample increased for a length  $L$  of 10 mm compared to the intact specimen. As the parallel pre-crack length  $L$  increased, the overall total number of acoustic emission events gradually decreased.

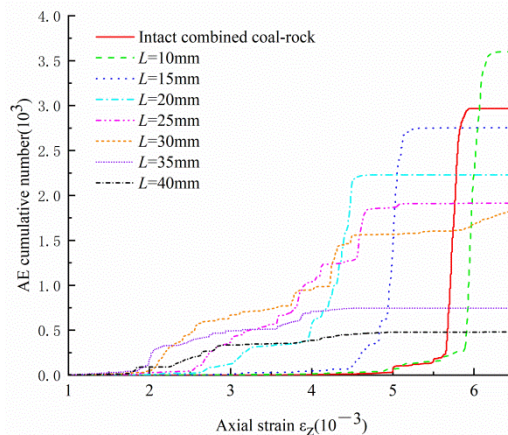


**Figure 15.** Effects of parallel pre-cracks at different lengths on acoustic emission characteristics.

Combined with the analysis of the macroscopic damage characteristics of the rock-coal combined body, the macroscopic damage characteristics of specimens 8 ( $\theta = 90^\circ$ ) and 9 ( $L = 10$  mm) indicate that only the coal sample ruptured, and the total number of acoustic emission events was higher than that of the intact specimen. As the parameters of the parallel pre-cracks changed, the total number of acoustic emission events also changed significantly, as the macroscopic damage characteristics changed from only the rock samples breaking to both coal and rock samples breaking. This suggests that parallel pre-cracks contribute to the generation of acoustic emissions under the same conditions.

The acoustic emission characteristics of specimens with three different macroscopic damage modes were selected separately for comparison. The macroscopic damage manifested in the form of coal sample damage, and the acoustic emission characteristics of specimen 1 are shown in Figure 16a; the macroscopic damage manifested in the form of both coal and rock damage, and the acoustic emission characteristics of parallel pre-crack specimen 7 containing an angle  $\theta$  of  $75^\circ$  and a length  $L$  of 30 mm are shown in Figure 16b. The acoustic emission characteristics of the parallel pre-crack specimen 11, containing an angle  $\theta$  of  $45^\circ$  and a length  $L$  of 20 mm, are shown in Figure 16c. The four photos

in each figure correspond to the linear–elastic stage, the compression–density stage, the elastic–plastic stage, and the damage stage, respectively.

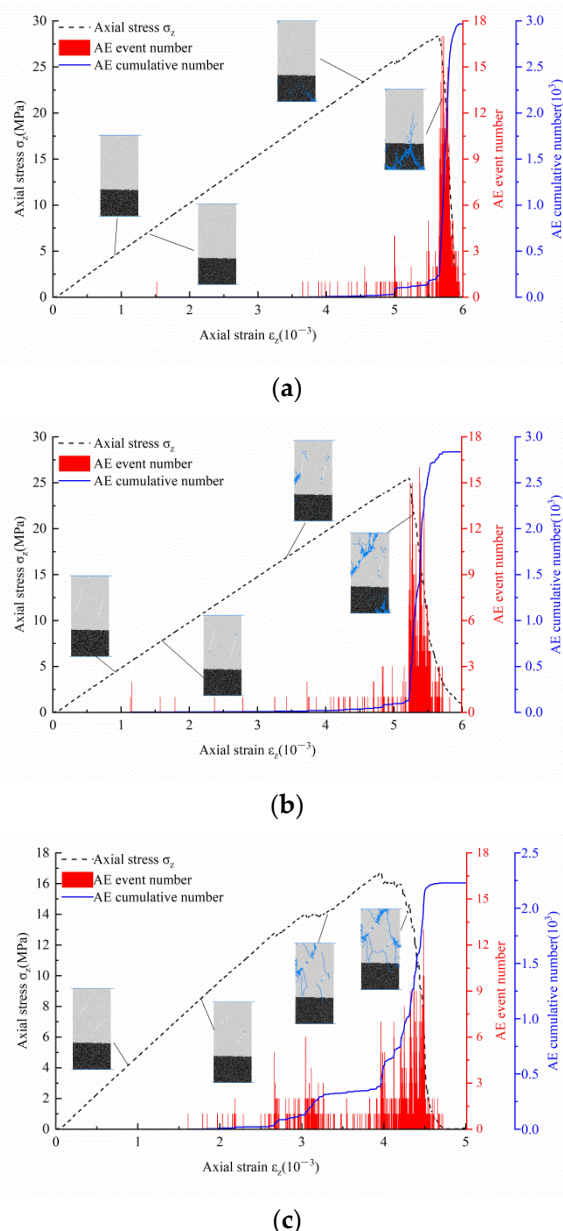


**Figure 16.** Acoustic emission characteristics of different macroscopic damage forms. (a) Acoustic emission characteristics of the macroscopic rupture form of coal rupture (specimen 1). (b) Acoustic emission characteristics of the macroscopic fracture form in which all the coal rock samples fractured (specimen 7). (c) Acoustic emission characteristics of the macroscopic fracture form where only the fracture of the rock sample occurred (specimen 11).

As shown in Figure 16a, only the specimens damaged by the coal sample showed no acoustic emission in the linear–elastic stage, a small amount of acoustic emission in the compression–density stage, and gradually increasing in the elastic–plastic stage; the greatest increase in the number of acoustic emission events was seen in the specimens after reaching peak intensity, with the number of acoustic emission events concentrated after the peak intensity. As shown in Figure 16b, in the specimens where both rock and coal were damaged, a small acoustic emission phenomenon appeared at the linear–elastic stage and the compression–density phase; the acoustic emission events gradually increased in the elasto-plastic phase, and a large acoustic emission phenomenon appeared after

reaching the peak intensity. The acoustic emission events were more evenly distributed compared to the intact specimens. As shown in Figure 16c, in the specimens with damaged rock samples, no acoustic emission events appeared in the linear–elastic stage, and they gradually appeared in the compression–density stage, becoming more prominent in the elastic–plastic stage, and concentrating after reaching the peak intensity. Compared with the intact specimen, the distribution of acoustic emission events was the most dispersed, with a large amount of acoustic emissions before and after the peak strain. As seen in Figure 16, the cumulative number of acoustic emission events for specimens containing parallel pre-cracks decreased compared with those for intact specimens. The highest total number of acoustic emission events was observed with coal sample damage, the second highest total number of acoustic emission events with both rock and coal damage, and the smallest total number of acoustic emission events with rock sample damage. Specimens containing parallel pre-cracks showed significantly more acoustic emissions in the elastic and plastic phases compared to the intact specimens, owing to their cracking at the tips of the parallel pre-cracks before reaching peak strength. After the peak strength was reached, the acoustic emissions of specimens containing parallel pre-cracks slowed down relative to the intact specimens, owing to the partial damage that occurred before the peak strength was reached.

## 5. Conclusions

(1) Parallel pre-cracks had a significant effect on the mechanical properties of the rock–coal combined body. Compared to the intact specimens, the stress–strain curve of the rock–coal combined body containing parallel pre-cracks changed significantly, with a decrease in peak strength, peak strain, elastic modulus, and cracking stress;

(2) The closer the angle  $\theta$  is to  $30^\circ$  and the longer the length  $L$  of the parallel pre-cracks, the lower the peak strength, peak strain, modulus of elasticity, and crack initiation stress of the specimen;

(3) For a rock–coal combined body with parallel pre-cracks, the macroscopic damage patterns are coal sample damage, coal–rock sample damage, and rock sample damage. The coal samples broke to different degrees with different parallel pre-crack parameters, and some showed no destruction;

(4) The rock–coal combined body with parallel pre-cracks exhibited three forms of crack initiation: crack initiation in the coal sample, simultaneous crack initiation at the tips of the parallel pre-cracks in the coal and rock samples, and crack initiation at the tips of the parallel pre-cracks in the rock sample.

**Author Contributions:** Conceptualization, Y.L.; methodology, J.L.; software, Y.L. and Q.Y.; validation, J.L.; data curation, Y.L.; writing—original draft preparation, Y.L.; writing—review and editing, J.L.; funding acquisition, J.L. All authors have read and agreed to the published version of the manuscript.

**Funding:** This work was supported by the Natural Science Foundation of Shandong Province China (grant number: ZR2022ME112, Jiangwei Liu).

**Institutional Review Board Statement:** Not applicable.

**Informed Consent Statement:** Not applicable.

**Data Availability Statement:** The data are available and explained in this article; readers can access the data supporting the conclusions of this study.

**Conflicts of Interest:** The authors declare no conflict of interest.

## References

- Chen, S.J.; Xia, Z.G.; Guo, W.J.; Shen, B.T. Research status and prospect of mining catastrophic response of rock mass under the influence of fault. *Coal Sci. Technol.* **2018**, *46*, 20–27. [[CrossRef](#)]
- Li, F.X.; Yin, D.W.; Zhu, C.; Wang, F.; Jiang, N.; Zhang, Z. Effects of Kaolin Addition on Mechanical Properties for Cemented Coal Gangue-Fly Ash Backfill under Uniaxial Loading. *Energies* **2021**, *14*, 3693. [[CrossRef](#)]

3. Chen, S.J.; Zhang, J.C.; Yin, D.W.; Cheng, X.Z.; Jiang, N. Relative permeability measurement of coal microchannels using advanced microchip technology. *Fuel* **2021**, *312*, 122633. [[CrossRef](#)]
4. Li, X.L.; Chen, S.J.; Wang, S.; Zhao, M.; Liu, H. Study on in situ stress distribution law of the deep mine taking linyi Mining area as an example. *Adv. Mater. Sci. Eng.* **2021**, *9*, 5594181. [[CrossRef](#)]
5. Deng, X.J.; Li, Y.; Wang, F.; Shi, X.M.; Yang, Y.C.; Xu, X.C.; Huang, Y.L.; Dewit, B. Experimental study on the mechanical properties and consolidation mechanism of microbial grouted backfill. *Int. J. Min. Sci. Technol.* **2022**, *32*, 271–282. [[CrossRef](#)]
6. Li, X.L.; Chen, S.J.; Liu, S.M.; Li, Z.H. AE waveform characteristics of rock mass under uniaxial loading based on Hilbert-Huang transform. *J. Cent. South Univ.* **2021**, *28*, 1843–1856. [[CrossRef](#)]
7. Liu, J.W.; Wu, N.; Si, G.Y.; Zhao, M.X. Experimental study on mechanical properties and failure behaviour of the pre-cracked coal-rock combination. *Bull Eng. Geol. Environ.* **2017**, *80*, 2307–2321. [[CrossRef](#)]
8. Kang, H.P. Seventy years development and prospects of strata control technologies for coal mine roadways in China. *Chin. J. Rock Mech. Eng.* **2021**, *40*, 1–30. [[CrossRef](#)]
9. Shi, X.D.; Bai, J.W.; Feng, G.R.; Wang, K.; Cui, B.Q.; Guo, J.; Yang, X.Y.; Song, C. Crack propagation law at the interface of FRP wrapped coal-backfilling composite structure. *Constr. Build. Mater.* **2022**, *344*, 128229. [[CrossRef](#)]
10. Dehghan, A.N.; Goshtasbi, K.; Ahangari, K.; Jin, Y. Experimental investigation of hydraulic fracture propagation in fractured blocks. *Bull Eng. Geol. Environ.* **2015**, *74*, 887–895. [[CrossRef](#)]
11. Kang, H.P.; Feng, Y.J. Hydraulic fracturing technology and its applications in strata control in underground coal mines. *Coal Sci. Technol.* **2017**, *45*, 1–9. [[CrossRef](#)]
12. Liu, J.W. Study on Change Mechanism and Control of Stress Field of Artificial Cracking Coal and Rock Mass. Ph.D. Thesis, China University of Mining, Xuzhou, China, 2021. [[CrossRef](#)]
13. Chen, S.J.; Li, Z.Y.; Ren, K.Q.; Feng, F.; Xia, Z.G. Experimental study on development process of reverse fault in coal measures strata and law of stress evolution in hanging wall strata. *J. Min. Saf. Eng.* **2020**, *37*, 366–375. [[CrossRef](#)]
14. Liu, C.; Zhang, D.M.; Zhao, H.G.; Li, M.H.; Song, Z.L. Experimental study on hydraulic fracturing properties of elliptical boreholes. *Bull Eng. Geol. Environ.* **2022**, *81*, 18. [[CrossRef](#)]
15. Chen, S.J.; Yin, D.W.; Zhang, B.L.; Ma, H.F.; Liu, X.Q. Mechanical characteristics and progressive failure mechanism of roof-coal pillar structure. *Chin. J. Rock Mech. Eng.* **2017**, *36*, 1588–1598. [[CrossRef](#)]
16. Chen, S.J.; Yin, D.W.; Jiang, N.; Wang, F.; Guo, W.J. Simulation study on effects of loading rate on uniaxial compression failure of composite rock-coal layer. *Geomech. Eng.* **2019**, *17*, 333–342. [[CrossRef](#)]
17. Guo, D.M.; Zuo, J.P.; Zhang, Y.; Yang, R.S. Research on strength and failure mechanism of deep coal-rock combination bodies of different inclined angles. *Rock Soil Mech.* **2011**, *32*, 1333–1339. [[CrossRef](#)]
18. Zuo, J.P.; Chen, Y.; Cui, F. Investigation on mechanical properties and rock burst tendency of differernt coal-rock combined bodies. *J. China Univ. Min. Technol.* **2018**, *47*, 81–87. [[CrossRef](#)]
19. Zhang, Z.T.; Liu, J.F.; Wang, L.; Liu, Z.J.; Yang, X.C. Effects of combination mode on mechanical properties and failure characteristics of the coal-rock combinations. *J. China Coal Soc.* **2012**, *37*, 841–847. [[CrossRef](#)]
20. Bai, J.W.; Feng, G.R.; WANG, Z.H.; Wang, S.Y.; Qi, T.Y.; Wang, P.F. Experimental Investigations on the Progressive Failure Characteristics of a Sandwiched Coal-Rock System Under Uniaxial Compression. *Appl. Sci.* **2019**, *9*, 1195. [[CrossRef](#)]
21. Zhao, D.C.; Xia, Y.J.; Zhang, C.Q.; Zhou, H.; Tang, C.A.; Liu, N.; Chen, J.; Wang, P.; Wang, C.I. Laboratory test and numerical simulations for 3D printed irregular columnar jointed rock masses under biaxial compression. *Bull Eng. Geol. Environ.* **2022**, *81*, 124. [[CrossRef](#)]
22. Xia, Y.J.; Liu, B.C.; Zhang, C.Q.; Liu, N.; Zhou, H.; Chen, J.; Tang, C.A.; Gao, Y.; Zhao, D.C.; Meng, Q.K. Investigations of mechanical and failure properties of 3D printed columnar jointed rock mass under true triaxial compression with one free face. *Geomech. Geophys. Geo-Energ. Geo-Resour.* **2022**, *8*, 26. [[CrossRef](#)]
23. Xia, Y.J.; Zhang, C.Q.; Zhou, H.; Hou, J.; Su, G.S.; Gao, Y.; Liu, N.; Singh, H.K. Mechanical behavior of structurally reconstructed irregular columnar jointed rock mass using 3D printing. *Eng. Geol.* **2020**, *268*, 105509. [[CrossRef](#)]
24. Reyes, O.; Einstein, H.H. Failure mechanisms of fractu-red rock: A fracture coalescence model. *Ism Congr.* **1991**, *V1*, 333–340.
25. Zhang, X.P.; Wong, L.N.Y. Cracking processes in rock-like material containing a single flaw under uniaxial compression: A numerical study based on parallel bonded-particle model approach. *Rock Mech. Rock Eng.* **2012**, *45*, 711–737. [[CrossRef](#)]
26. Tang, Q.; Li, Y.A. Particle Flow Simulation on the Influence of Confinement on Crack Propagation in pre-cracked rock. *J. Yangtze River Sci. Res. Inst.* **2015**, *32*, 81–85.
27. Yin, D.W.; Chen, S.J.; Liu, X.Q.; Wang, G.; Ma, H.F.; Shen, B.T. Particle Flow Simulation of Effects of Joint Characteristics on Crack Initiation Stress and Crack Damage Stress of Jointed Granite. *J. Basic Sci. Enginee. Ring* **2018**, *26*, 808–820. [[CrossRef](#)]
28. Zhang, X.L. Research on Crack Initiation and Propagation Characteristics of Disc Specimens Containing a Parallel Prefabricated Double Cracks. Master’s Thesis, Henan Polytechnic University, Jiaozuo, China, 2020. [[CrossRef](#)]
29. Yang, S.Q. Crack coalescence behavior of brittle sandstone samples containing two coplanar fissures in the process of deformation failure. *Eng. Fract. Mech.* **2011**, *78*, 3059–3081. [[CrossRef](#)]
30. Yang, S.Q.; Wen, S.; Li, L.Q. Experimental study on deformation and strength properties of coarse marble with discontinuous pre-existing cracks under different confining pressures. *Chin. J. Rock Mech. Eng.* **2007**, *26*, 1572–1587.
31. Yang, S.Q.; Dai, Y.H.; Han, L.J.; He, Y.N.; Li, Y.S. Uniaxial compression experimental research on deformation and failure properties of brittle marble specimen with pre-existing fissures. *Chin. J. Rock Mech. Eng.* **2009**, *28*, 2391–2404.

32. Yang, S.Q.; Huang, Y.H.; Wen, S. Experimental study of mechanical behavior of red sandstone with two non-coplanar fissures after high temperature heating. *Chin. J. Rock Mech. Eng.* **2015**, *34*, 440–451. [[CrossRef](#)]
33. Xie, L.F.; Zhu, Q.Y.; Qin, Y.J.; Wang, J.H.; Qian, J.G. Study on evolutionary characteristics of toppling deformation of anti-dip bank slope based on energy field. *Sustainability* **2020**, *12*, 7544. [[CrossRef](#)]
34. Chen, S.J.; Ge, Y.; Yin, D.W.; Yang, H.S. An experimental study of the uniaxial failure behaviour of rock-coal composite samples with pre-existing cracks in the coal. *Adv. Civ. Eng.* **2019**, *2019*, 8397598. [[CrossRef](#)]
35. Zhang, X.P.; Wong, L.N.Y. Crack initiation propagation and coalescence in rock-like material containing two flaws: A numerical study based on bonded-particle model approach. *Rock Mech. Rock Eng.* **2013**, *46*, 1001–1021. [[CrossRef](#)]
36. Kong, X.G.; He, D.; Liu, X.F.; Wang, E.Y.; Li, S.G.; Liu, T.; Ji, P.F.; Deng, D.Y.; Yang, S.R. Strain characteristics and energy dissipation laws of gas-bearing coal during impact fracture process. *Energy* **2022**, *242*, 123038. [[CrossRef](#)]
37. Shen, J.Y.; Zhan, S.X.; Karakus, M.; Zuo, J.P. Effects of flaw width on cracking behavior of single-flawed rock specimens. *Bull Eng. Geol. Environ.* **2021**, *80*, 1701–1711. [[CrossRef](#)]
38. Ma, J.B.; Jiang, N.; Wang, X.J.; Jia, X.D.; Yao, D.H. Numerical study of the strength and characteristics of sandstone samples with combined double hole and double fissure defects. *Sustainability* **2021**, *13*, 7090. [[CrossRef](#)]
39. Kong, X.G.; Li, S.G.; Wang, E.Y.; Wang, X.; Zhou, Y.X.; Ji, P.F.; Shuang, H.Q.; Li, S.R.; Wei, Z.Y. Experimental and numerical investigations on dynamic mechanical responses and failure process of gas-bearing coal under impact load. *Soil Dyn. Earthq. Eng.* **2021**, *142*, 106579. [[CrossRef](#)]
40. Liu, J.W.; Liu, C.Y.; Yao, Q.L.; Si, G.Y. The position of hydraulic fracturing to initiate vertical fractures in hard hanging roof for stress relief. *Int. J. Rock Mech. Min. Sci.* **2020**, *132*, 104328. [[CrossRef](#)]